

# Energy Advances

Accepted Manuscript

This article can be cited before page numbers have been issued, to do this please use: H. Patel, A. K. Mohanty and M. Misra, *Energy Adv.*, 2024, DOI: 10.1039/D4YA00305E.



This is an Accepted Manuscript, which has been through the Royal Society of Chemistry peer review process and has been accepted for publication.

Accepted Manuscripts are published online shortly after acceptance, before technical editing, formatting and proof reading. Using this free service, authors can make their results available to the community, in citable form, before we publish the edited article. We will replace this Accepted Manuscript with the edited and formatted Advance Article as soon as it is available.

You can find more information about Accepted Manuscripts in the [Information for Authors](#).

Please note that technical editing may introduce minor changes to the text and/or graphics, which may alter content. The journal's standard [Terms & Conditions](#) and the [Ethical guidelines](#) still apply. In no event shall the Royal Society of Chemistry be held responsible for any errors or omissions in this Accepted Manuscript or any consequences arising from the use of any information it contains.

# Sustainable synthesis of activated porous carbon from lignin for enhanced CO<sub>2</sub> capture: A comparative study of physicochemical activation routes

View Article Online  
DOI: 10.1039/C4YA00305E

Himanshu Patel,<sup>ab</sup> Amar Mohanty,<sup>ab</sup> Manjusri Misra<sup>\*ab</sup>

<sup>a</sup> Bioproducts Discovery and Development Centre, Department of Plant Agriculture, University of Guelph, Crop Science Building, Guelph, Ontario N1G 2W1, Canada

<sup>b</sup> School of Engineering, University of Guelph, Thornbrough Building, 80 South Ring Road E, Guelph, Ontario N1G 2W1, Canada

\* E-mail addresses: [mmisra@uoguelph.ca](mailto:mmisra@uoguelph.ca) (M. Misra)

## Abstract

A sustainable and readily available material-lignin protobind 2400 was upcycled to activated porous carbon (APC) compatible with post-combustion CO<sub>2</sub> capture. The effectiveness of the novel two-step physicochemical activation using KOH + CO<sub>2</sub> and ZnCl<sub>2</sub> + CO<sub>2</sub> was compared with that of the respective physical (only CO<sub>2</sub>) and chemical activation (only KOH or ZnCl<sub>2</sub>). The effect of carbonization conditions (N<sub>2</sub> or CO<sub>2</sub> purging) on the resulting APC properties and CO<sub>2</sub> adsorption performance was studied. The maximum BET surface area of 1480 m<sup>2</sup>/g and the best CO<sub>2</sub> adsorption capacity of 5.68, 3.66, and 2.67 mmol/g were observed at 0, 25, and 40 °C/1 bar, respectively. From the precursor to the final product, the APC yield falls within the range of 14.5-40.8 wt.%. The APC derived from lignin exhibited better CO<sub>2</sub>/N<sub>2</sub> selectivity. The isosteric heat of adsorption for all the APCs remained below 40 kJ/mol, which suggested a lower energy requirement during the regeneration. The excellent reusability with fluctuations of only 0.51% in the amount of CO<sub>2</sub> adsorbed over ten consecutive adsorption/desorption cycles, highlights the APC's outstanding recyclability.

**Keywords:** Carbon capture, Activated porous carbon, Physicochemical activation, Waste valorization

## Nomenclature

GHGs	Greenhouse Gases
CCUS	Carbon Capture, Utilization, and Storage
APC	Activated Porous Carbon
BET	Brunauer-Emmett-Teller
<i>L</i>	Lignin Protobind 2400
NLPH	Normal Litres per Hour
<i>L X-Y</i>	Lignin prtobind 2400 based activated porous carbon, where <i>X</i> represents gas purged during carbonization and <i>Y</i> denotes activating agent used; <i>X</i> = <i>N</i> indicates N <sub>2</sub> purging, <i>X</i> = <i>CD</i> indicates CO <sub>2</sub> purging; <i>Y</i> = <i>K</i> denotes KOH



activation,  $Y = CD$  denotes  $\text{CO}_2$  activation,  $Y = Z$  denotes  $\text{ZnCl}_2$  activation,  $Y = ZCD$  denotes  $\text{KOH} + \text{CO}_2$  activation,  $Y = ZCD$  denotes  $\text{ZnCl}_2 + \text{CO}_2$  activation

SD	Standard Deviation
SEM	Scanning Electron Microscopy
TEM	Transmission Electron Microscopy
HR-TEM	High-resolution Transmission Electron Microscopy
NLDFT	Non-local Density Functional Theory
$S_{\text{BET}}$	Specific BET surface area, $\text{m}^2/\text{g}$
$S_{\text{micro}}$	Micro-pore area using t-plot method, $\text{m}^2/\text{g}$
$\phi_{\text{micro}}$	Micro-porosity ( $S_{\text{micro}}/S_{\text{BET}} \times 100$ ), %
$R_{\text{avg}}$	Average pore radius, nm
$V_{\text{T}}$	Estimated at a relative pressure $P/P_0 = 0.99$ , $\text{cm}^3/\text{g}$
$V_{\text{micro}}$	Micropore volume estimated using t-plot method, $\text{cm}^3/\text{g}$
$f_{\text{micro}}$	Percentage of micro-pore volume ( $V_{\text{micro}}/V_{\text{T}} \times 100$ ), %
$q_{\text{st}}$	Isothermic heat of adsorption, $\text{kJ}/\text{mol}$

## 1 Introduction

Climate change is closely tied to the continuous increase in anthropogenic greenhouse gases (GHGs) emissions and poses a significant threat to human existence. The energy sector, driven by hefty dependence on fossil fuels, is accountable for 72% of GHGs, with  $\text{CO}_2$  contributing 76% to the overall GHGs emissions.<sup>1</sup> Despite a noteworthy increase in renewables, fossil fuels are projected to maintain a substantial global dependence of 74% by 2040, underscoring the critical need to decarbonize the energy sector.<sup>2</sup> This highlights the significance of  $\text{CO}_2$  as the most crucial greenhouse gas (GHG) contributing to catastrophic events, such as climate change associated with global warming, increased ocean acidity, and rising sea levels. The World Meteorological Organization's report highlights that the socioeconomic consequences of climate change are worsening, with unprecedented GHG concentrations pushing global temperatures perilously closer to critical levels.<sup>3</sup> The primary aim of the Paris Climate Change Agreement is to achieve a 40% reduction in GHG emissions by 2030.<sup>4</sup> To address the immediate challenges posed by the escalating levels of global  $\text{CO}_2$  concentration, there is an ongoing exploration of carbon capture, utilization, and storage (CCUS) as a potential short-term solution to curb the release of this specific greenhouse gas. Fundamentally, carbon capture involves the application of technologies to either directly extract  $\text{CO}_2$  from the air/atmosphere or to capture it during the formation process (large point source). Specifically, the removal of  $\text{CO}_2$  from a flue gas stream is termed post-combustion  $\text{CO}_2$  capture, which can be a cost-effective approach for addressing emissions from current coal and gas-fired power plants, as well as coal-intensive industries, such as cement, oil refineries, chemicals, and steel.<sup>5</sup> Approximately one-third of the existing coal and gas-fired power plants have been constructed in the last decade. Retrofitting these facilities with post-combustion  $\text{CO}_2$  capture enables them to remain operational, thereby avoiding the expenses associated with early phase shutdowns.<sup>6</sup>



Several methods such as amine absorption, membrane separation, cryogenic distillation, and physical adsorption have been developed for CO<sub>2</sub> capture from industrial flue gases. The adsorption-based method, utilizing solid adsorbents such as porous aluminosilicate or zeolites, metal organic frameworks, silica gel, and activated porous carbons (APCs) offers excellent performance and energy efficiency compared to other separation techniques.<sup>7,8</sup> In this context, APCs present numerous advantages over other CO<sub>2</sub> adsorbents. Their affordability, well-developed pore structure, exceptional thermal and chemical stability, heightened efficiency under humid conditions, straightforward surface functionalization, and lower energy requirements during regeneration highlight their significance as CO<sub>2</sub> adsorbents coupled with commendable multi-cyclic stability.<sup>9,10</sup> Presently, large-scale production of APCs predominantly relies on carbon-intensive precursors, such as coal, as well as carbon-neutral alternatives, such as wood and coconut shells.<sup>11</sup> Researchers are exploring economically viable and efficient replacements to mitigate the environmental impact of this sector and fortify the supply chain.<sup>12</sup>

On the other hand, lignin stands as the Earth's second most abundant naturally occurring complex organic material. Lignocellulosic wastes (forest and agricultural waste) and pulp paper mills are two potential sources of lignin, generating 225 and 130 Mt of lignin per annum, respectively.<sup>13</sup> Projections indicate that this figure will surge by 225 Mt per year by 2030, driven by the increasing annual production of lignin as a by-product of bioethanol production mandated by the Renewable Fuel Standard (RFS) program aimed at 60 billion gallons of biofuel.<sup>14</sup> Hence, the development of cost-effective valorisation technologies is crucial to ensure the long-term stability and vitality of biorefineries. Traditionally regarded as a low-value waste by-product, recent studies have demonstrated its potential in producing high-value commodities.<sup>15–19</sup> Despite an expanding body of research on the conversion of lignin into commercial commodities, a large fraction of lignin produced by the paper industry is currently incinerated as a low-value fuel for electricity and heat generation (with a value of < \$50/dry ton).<sup>20,21</sup> Less than 2% is used to produce specialty chemicals and other value-added products. The advancement of value-added lignin-derived co-products holds the potential to enhance the profitability of second-generation biorefineries and the paper industry by valorising their lignin by-products.

Physical and chemical activation are the most common and extensively studied techniques for producing APCs. Their individual effects on the performance and properties of APCs prepared from a wide range of carbonaceous materials have been investigated extensively. A hybrid synthesis route of physicochemical activation that simultaneously utilize both physical and chemical activating agents is less explored. Previously, some researchers investigated the effect of physicochemical activation on other applications, such as Cu adsorption<sup>22</sup>, dye (i.e., crystal violet) removal<sup>23</sup>, and CH<sub>4</sub> storage<sup>24</sup>. The effect of physicochemical activation on the CO<sub>2</sub> adsorption performance is even less studied among other applications of APCs. Previous studies have reported the preparation of APC via physicochemical activation using ZnCl<sub>2</sub> + CO<sub>2</sub><sup>25</sup> and KOH + CO<sub>2</sub><sup>26,27</sup> for CO<sub>2</sub> adsorption. However, these studies lacked a comparison of the effectiveness of physicochemical activation with the respective physical and chemical



reagents used. In our previous study, we compared the CO<sub>2</sub> adsorption performance of APCs derived through physicochemical activation of pine sawdust with those derived through chemical activation (using only KOH) and physical activation (using only CO<sub>2</sub>).<sup>28</sup> Physicochemical activation (KOH + CO<sub>2</sub>) resulted in APCs with 68% and 586% more BET surface area compared to APCs derived using only KOH and only CO<sub>2</sub> activation, respectively. However, the CO<sub>2</sub> adsorption capacity of physicochemically activated carbon was 26.5% lower than that of APCs produced using only KOH and 53.3% higher than that of APCs produced using only CO<sub>2</sub> activation. However, a limitation of this study was that it tested only one combination of physical and chemical activating reagents. The results may be significantly different for different combinations and feedstocks.

In this study, the combined effects of chemical activating agents (such as KOH and ZnCl<sub>2</sub>) and a physical activating agent (CO<sub>2</sub>) on the textural properties and CO<sub>2</sub> adsorption performance of the resulting APC were investigated. In addition, we compared the effectiveness of physicochemical activation with that of individual chemical and physical activating agents. The effect of carbonization conditions on APC performance was also studied. Lignin protobind 2400, a sustainable material, was used as a precursor to derive APC for CO<sub>2</sub> capture applications.

## 2 Experimental

### 2.1 Feedstock and material

Lignin protobind 2400 (*L*) was purchased from ALM Private Limited, Hoshiarpur, Punjab, India. The chemical and thermal properties of *L* were reported previously.<sup>29</sup> KOH pellets (P250-3) with a purity of  $\geq 85.0\%$ , anhydrous ZnCl<sub>2</sub> with a purity of  $\geq 98.0\%$ , and 1 N HCl solution (SA48-1) from Fisher Scientific were used.

### 2.2 Synthesis of activated porous carbon

A horizontal fixed-bed annealing furnace (Carbolite GERO, GLO 10/11-1G) was used for carbonization and activation. More details on the furnace used have been published elsewhere.<sup>28</sup> APCs were produced by direct activation as well as two-step activation. KOH, ZnCl<sub>2</sub>, CO<sub>2</sub>, and their combinations were used as the activating agents. Based on the type of activating agent used, the activation can be classified into three categories: (i) physical activation using CO<sub>2</sub>, (ii) chemical activation utilizing KOH and ZnCl<sub>2</sub>, and (iii) physicochemical activation using KOH + CO<sub>2</sub> and ZnCl<sub>2</sub> + CO<sub>2</sub>. Figure 1 illustrates the methodology followed during the APC preparation. The precursors were dried in a hot-air oven at 80 °C for 24 h, prior to carbonization and/or activation. Lignin protobind 2400 was carbonized at 600 °C, with a heating rate of 7.5 °C/min of a heating rate and a residence time of 1.5 h in an N<sub>2</sub> atmosphere (at 50 NLPH). The reactor was allowed to cool down naturally and the resulting biochar was labelled as *L N*. Pore formation via CO<sub>2</sub> mainly occurs via Boudouard reaction, which activates above 700 °C.<sup>30</sup> Considering the poor thermal



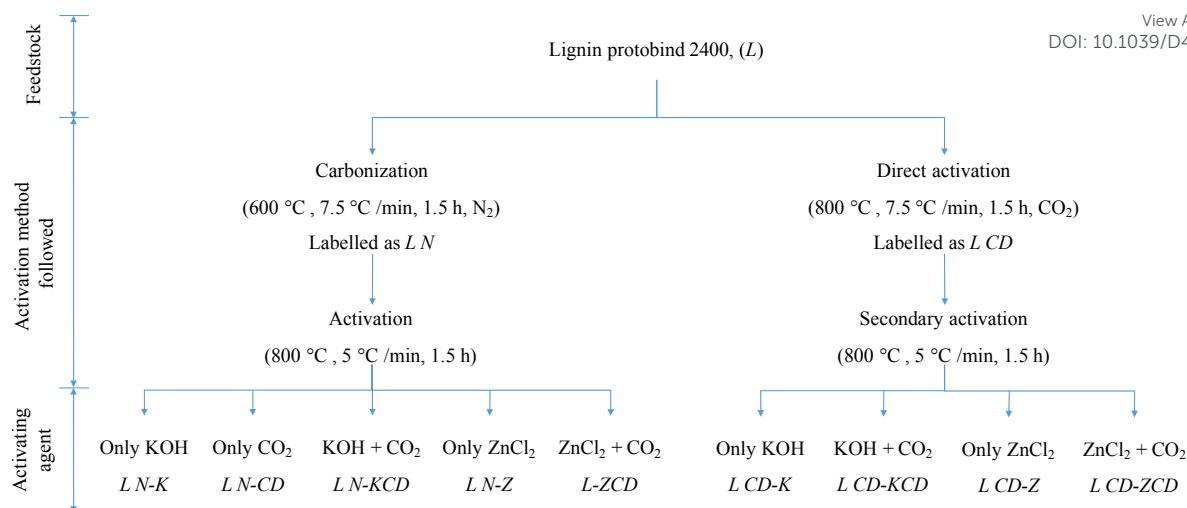
conductivity of the feedstock used and the heat transfer limitations of the reactor housing, all activation experiments were performed at 800 °C. Direct physical activation of lignin protobind 2400 was performed at 800 °C, 7.5 °C/min of a heating rate, 1.5 h of a residence time in a CO<sub>2</sub> atmosphere (at 75 NLPH). The reactor was cooled naturally, and the resulting biochar was labelled *L CD*. For all CO<sub>2</sub> related activations, the precursors were heated from room temperature to 800 °C in an N<sub>2</sub> environment (at 50 NLPH). After achieving 800 °C, N<sub>2</sub> purging was stopped, and CO<sub>2</sub> was purged (at 75 NLPH) throughout the holding time of 1.5 h and until the reactor temperature dropped below 700 °C during the natural cool-down cycle. From 700 °C to room temperature N<sub>2</sub> was purged.

Directly activated APC (i.e., *L CD*) and biochar (i.e., *L N*) were pulverized in a ball mill (Fritsch, Pulverisette 5) for 1 h and sieved through 300 μm mesh. Prior to chemical and physicochemical activation, 25 g of the pulverized precursor was impregnated with 50 g of KOH or ZnCl<sub>2</sub>, and 150 ml of deionized water was added. The slurry was stirred for 24 h at 500 RPM followed by overnight drying in a hot-air oven at 105 °C. The dried and impregnated samples were activated at 800 °C, with a heating rate of 5 °C/min for 1.5 h. Adhering KOH or ZnCl<sub>2</sub> was removed from the derived APCs via hot water washing, followed by acid soaking in 0.1 M HCl, and then further hot water washing until a neutral pH was achieved. The washed APCs were dried at 105 °C for 24 h, labelled, and stored. The yield was calculated based on the initial and final weight differences. The combined yield of the carbonization and activation steps was considered as the APC yield.

*L X-Y* denotes the lignin protobind 2400 based activated porous carbon. Where *X* denotes the type of purging gas used during carbonization: *X = N* indicates carbonization was executed in N<sub>2</sub> and *X = CD* indicates carbonization was performed in CO<sub>2</sub> atmosphere. *Y* denotes the type of activating agent used in the two-step activation process: *Y = K* indicates KOH used as an activating agent, *Y = CD* denotes CO<sub>2</sub> used as an activating agent, *Y = Z* means ZnCl<sub>2</sub> is used as an activating agent, *Y = KCD* means KOH + CO<sub>2</sub> is used as the activating agent, and *Y = ZCD* is ZnCl<sub>2</sub> + CO<sub>2</sub> used as the activating agent. For example, *L N-KCD* represents lignin protobind 2400 based activated carbon derived via a two-step activation method from lignin protobind 2400 biochar prepared in a N<sub>2</sub> atmosphere, followed by activation using KOH + CO<sub>2</sub> as an activating agent. The details of the characterization protocol have been explained elsewhere.<sup>28,31</sup>







View Article Online  
DOI: 10.1039/D4YA00305E

**Figure 1.** Methodology followed during the synthesis of activated porous carbon. ( $L X-Y$ , where  $X$  represents gas purged during carbonization and  $Y$  denotes activating agent used;  $X = N$  indicates  $N_2$  purging,  $X = CD$  indicates  $CO_2$  purging;  $Y = K$  denotes KOH activation,  $Y = CD$  denotes  $CO_2$  activation,  $Y = Z$  denotes  $ZnCl_2$  activation,  $Y = KCD$  denotes KOH +  $CO_2$  activation,  $Y = ZCD$  denotes  $ZnCl_2$  +  $CO_2$  activation).

### 3 Result and discussion

#### 3.1 Composition and structural characterization

The elemental compositions of lignin protobind 2400, biochar, and APCs are listed in Table 1. Carbonization significantly increased the carbon content and reduced the hydrogen and oxygen content. Chemical activation using KOH and physical activation using  $CO_2$  produced APC with slightly higher carbon content than biochar. However, chemical activation using  $ZnCl_2$  and physicochemical activation ( $KOH + CO_2$  and  $ZnCl_2 + CO_2$ ) significantly reduced the carbon content compared to biochar. Similar trends were observed during physicochemical activation (using  $KOH + CO_2$ ) of pine sawdust.<sup>28</sup> Compared to the feedstock, the reduced H/C molar ratio for the biochar and APCs indicated that the aromatization reaction was dominant during carbonization and activation.

Table 1. Elemental composition of the feedstock, biochar, and activated porous carbons.

Material	C, wt.%	H, wt.%	N, wt.%	O <sup>a</sup> , wt.%	H/C	C/O	H/O
<i>L</i>	63.03	6.20	1.23	29.54	1.18	2.85	3.36
	SD = 0.23	SD = 0.01	SD = 0.00	SD = 0.22			
<i>LN</i>	84.84	2.45	1.13	11.58	0.35	9.77	3.39
	SD = 0.09	SD = 0.01	SD = 0.98	SD = 0.95			
<i>LN-K</i>	85.05	0.32	0.68	13.95	0.05	8.13	0.37
	SD = 0.30	SD = 0.03	SD = 0.02	SD = 0.27			
<i>LCD-K</i>	87.25	1.02	0.78	10.95	0.14	10.62	1.49
	SD = 0.63	SD = 0.01	SD = 0.01	SD = 0.62			



<i>L N-CD</i>	86.17 SD = 1.79	1.15 SD = 0.10	1.12 SD = 0.13	11.56 SD = 1.95	0.16	9.94	1.50
<i>L CD</i>	85.91 SD = 1.05	0.79 SD = 0.09	1.30 SD = 0.15	12.00 SD = 1.27	0.11	9.55	1.05
<i>L N-KCD</i>	81.86 SD = 1.41	0.51 SD = 0.16	1.22 SD = 0.22	16.41 SD = 1.77	0.07	6.65	0.50
<i>L CD-KCD</i>	81.10 SD = 1.14	1.16 SD = 0.03	1.20 SD = 0.01	16.53 SD = 1.13	0.17	6.54	1.12
<i>L N-Z</i>	76.24 SD = 6.36	0.84 SD = 0.15	0.66 SD = 0.02	22.25 SD = 6.53	0.13	4.57	0.61
<i>L N-ZCD</i>	76.11 SD = 4.67	0.93 SD = 0.13	0.61 SD = 0.04	22.35 SD = 4.80	0.15	5.93	0.90
<i>L CD-Z</i>	80.22 SD = 1.55	1.01 SD = 0.09	0.74 SD = 0.02	18.03 SD = 1.65	0.15	5.93	0.90
<i>L CD-ZCD</i>	80.37 SD = 2.81	1.06 SD = 0.13	0.67 SD = 0.05	17.90 SD = 2.94	0.16	5.99	0.95

<sup>a</sup> by differences

SD = Standard deviation

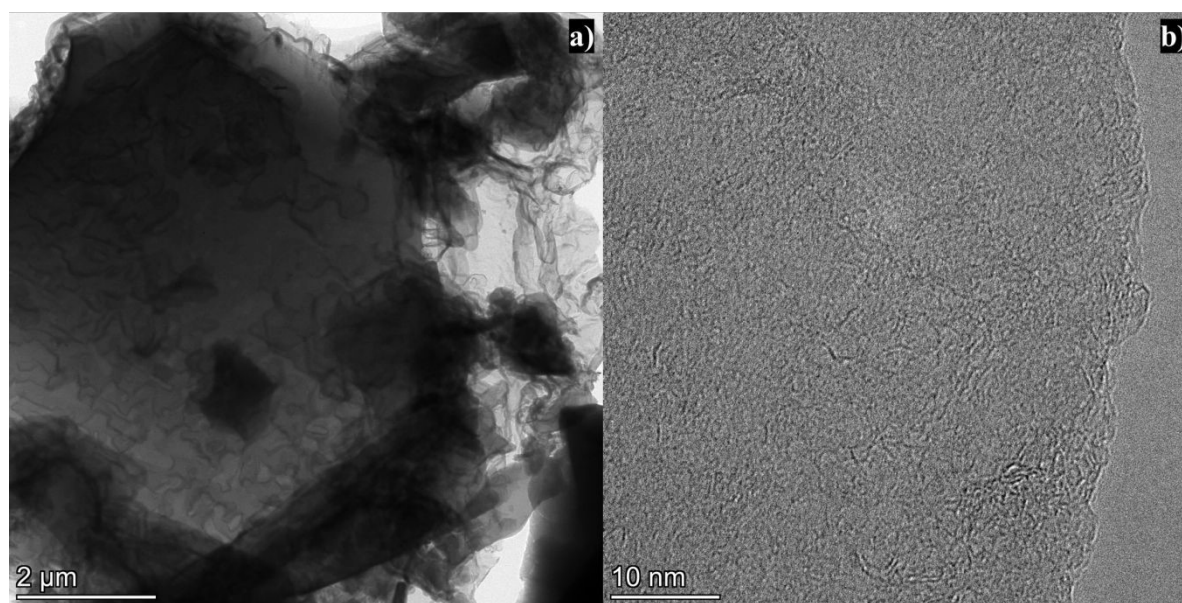


**Figure 2.** (a) Transmission electron micrograph and (b) High-resolution transmission electron micrograph of *L N-K*.

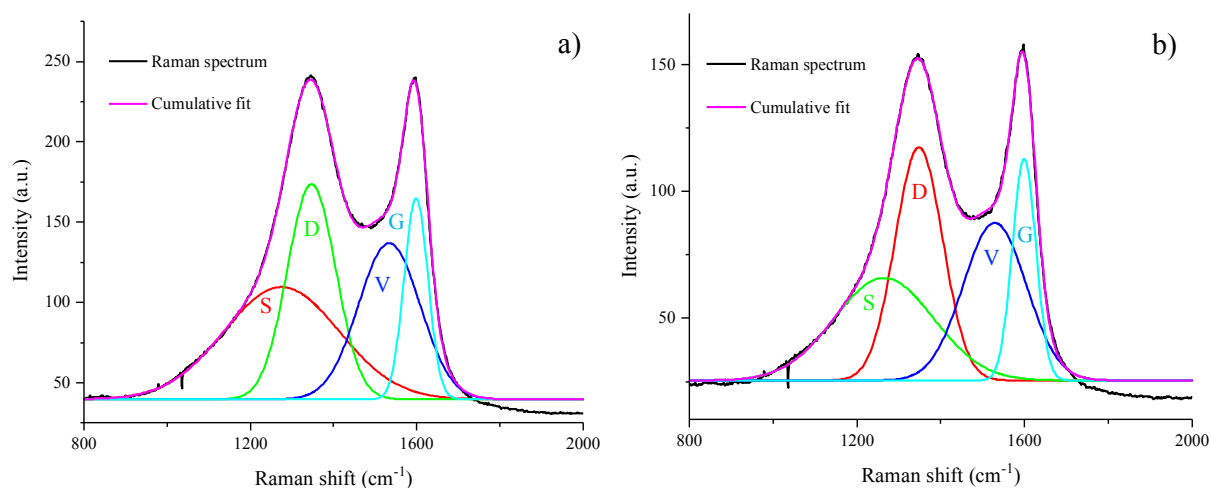
Scanning electron microscopy (SEM) was utilized to investigate the morphology of the lignin protobind 2400 based APCs. SEM micrographs of all lignin-based APCs are presented in Figure S1, indicating a blocky and sharp edge morphology. Random cracks and cavities were observed on the external surface. The porous structure and detailed morphology of *L N-K* were further investigated using transmission electron microscopy (TEM) and high-resolution transmission electron microscopy (HR-TEM). As portrayed in Figure 2a, the overlapping of multiple carbon sheets resulted in a relatively dense TEM image. The HR-TEM image of *L N-K* depicted in Figure 2b shows disordered worm-like micropores randomly distributed on the

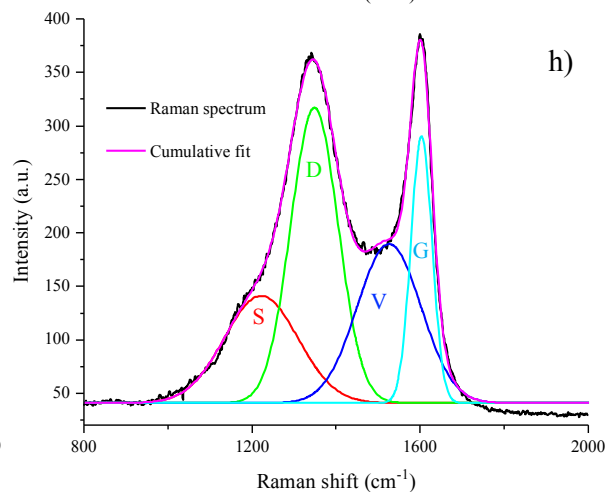
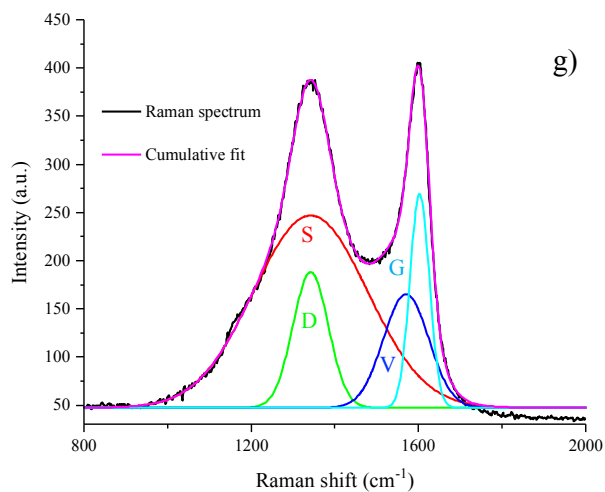
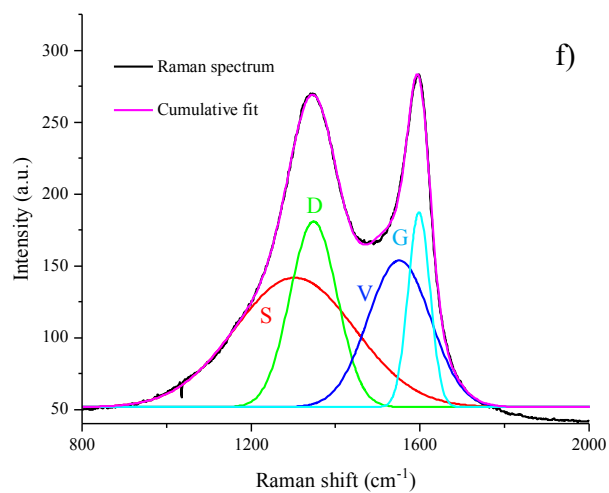
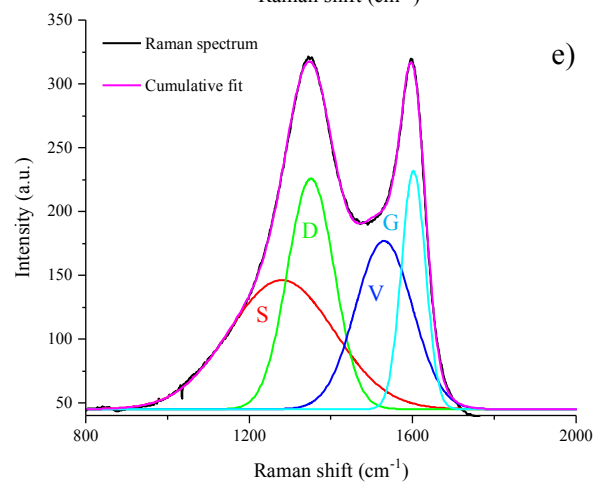
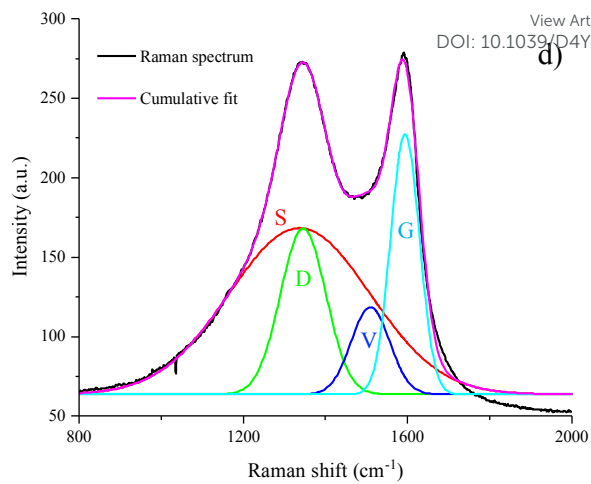
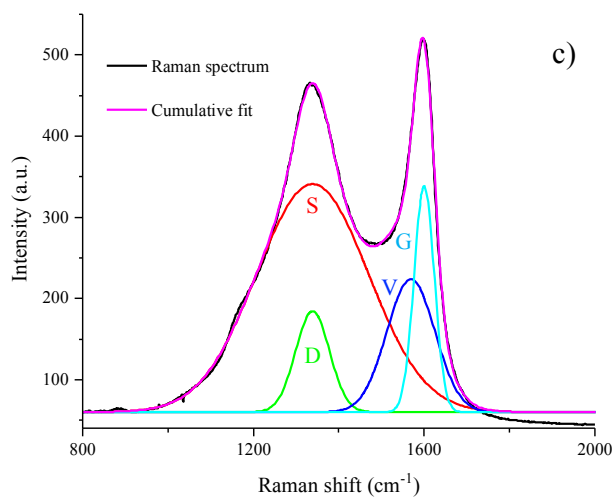




surface of *L N-K*, indicating a microporous nature, which was further confirmed by  $N_2$  adsorption isotherms.

Raman spectra were recorded to evaluate crystallographic disorders in carbon structure. Only the key features of the Raman spectra within the Raman shift range of 800–2000  $\text{cm}^{-1}$  are highlighted in Figure 3. Two broad overlapping peaks were deconvoluted using the Fourier–Gaussian peak-fitting method. The first peak, a maxima occurring at  $\sim 1300 \text{ cm}^{-1}$ , represents a defect or disorder in the carbon structure originating from local defects (D-band). The second peak at  $\sim 1600 \text{ cm}^{-1}$  can be attributed to the graphitic crystallites of  $\text{sp}^2$  hybridized carbon (G-band). The  $I_D/I_G$  ratio is the intensity ratio of the D and G peaks, which quantifies the degree of graphitization. This signifies the ratio of disordered carbon structure to ordered carbon structure. A lower  $I_D/I_G$  ratio indicates a more ordered or crystalline carbon structure. Figure 3k portrays the  $I_D/I_G$  ratios of all ten APCs. Physical activation resulted in the most ordered carbon structure morphologically, which is consistent with a previous study using different feedstocks.<sup>28</sup> Chemical or physicochemical activation leads to pronounced deformation of the aromatic rings, which reduces the degree of graphitization. During activation,  $\text{ZnCl}_2$  was more reactive towards the aromatic rings of biochar produced in a  $\text{CO}_2$  atmosphere than in a  $\text{N}_2$  atmosphere. This can be inferred from the higher  $I_D/I_G$  ratio for *L N-Z* than for *L CD-Z* and *L N-ZCD* than for *L CD-ZCD*. Conversely,  $\text{KOH}$  was more reactive towards aromatic rings of biochar produced in a  $\text{N}_2$  atmosphere than in a  $\text{CO}_2$  atmosphere. The higher  $I_D/I_G$  ratio for *L N-K* than for *L CD-K* and *L N-KCD* than for *L CD-KCD* support this statement.





View Article Online  
DOI: 10.1039/D4YA00305E



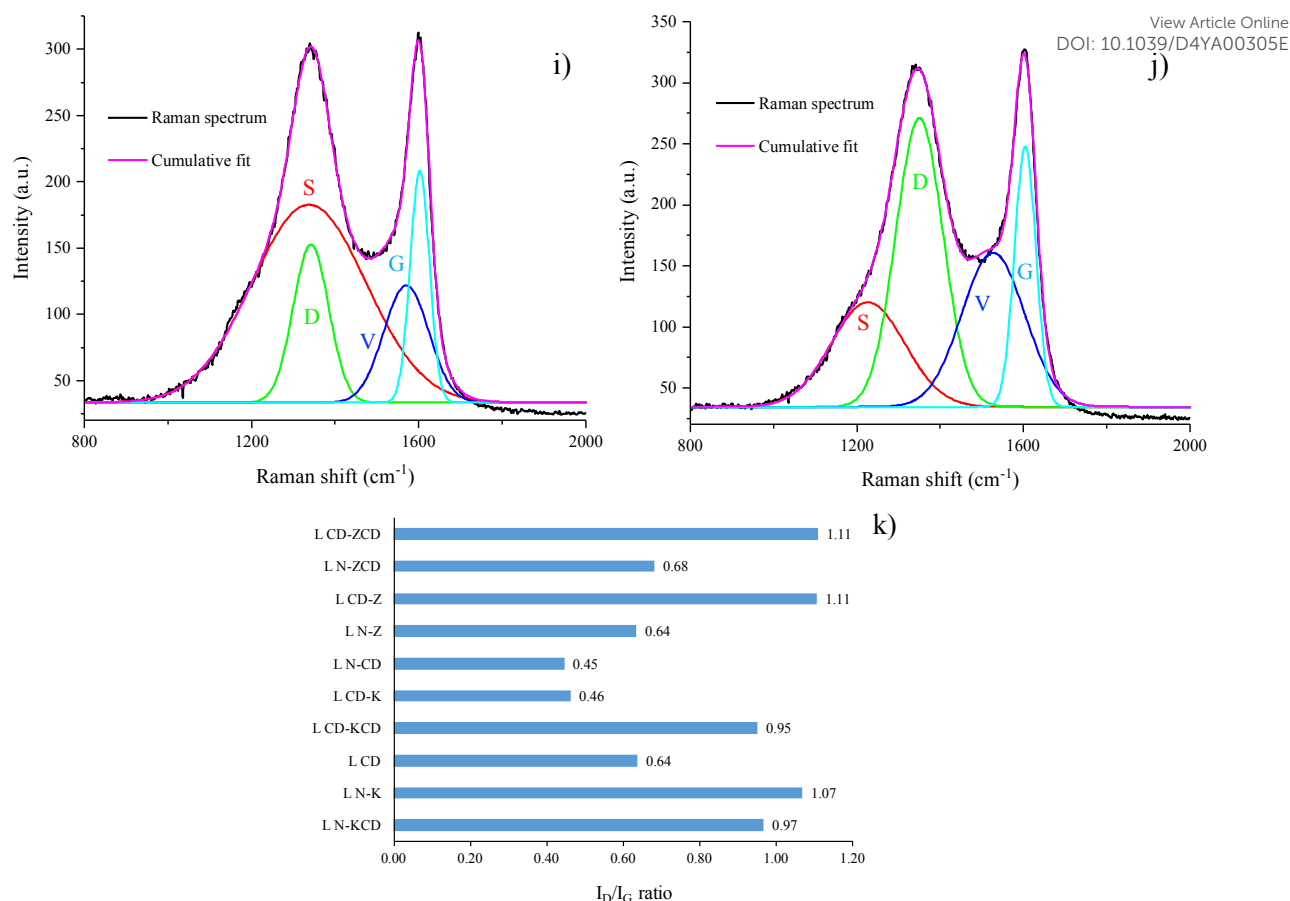


**Figure 3.** Curve fitting of Raman Spectra (a) *L N-K*, (b) *L CD-K*, (c) *L N-CD*, (d) *L CD*, (e) *L N-KCD*, (f) *L CD-KCD*, (g) *L N-Z*, (h) *L CD-Z*, (i) *L N-ZCD*, (j) *L CD-ZCD*, (k)  $I_D/I_G$  ratio.

### 3.2 Textural properties

The textural properties of the carbonaceous adsorbent significantly affect its CO<sub>2</sub> adsorption performance. Therefore, to evaluate the porosity, N<sub>2</sub> adsorption isotherms were recorded at -196 °C up to a relative pressure of 1.0 bar. Figure 4a shows the N<sub>2</sub> adsorption isotherms of lignin-based APCs prepared using a wide range of activating agents. For all the samples, a steep rise in N<sub>2</sub> adsorption was observed at  $P/P_0 < 0.05$ . The rise ranged from 65 to 333 cc/g, which could be attributed to micropore filling due to better adsorbent-adsorbate interactions at lower pressures.<sup>32,33</sup> Thereafter, beyond  $P/P_0 = 0.05$ , the N<sub>2</sub> adsorption increased gradually, except for *L N-KCD*. For *L N-KCD*, N<sub>2</sub> adsorption continued to rise exponentially up to a  $P/P_0$  of 0.45 and achieved plateau. For all the samples, hysteresis at  $P/P_0 > 0.4$  suggested a type IV isotherm according to IUPAC classification. The existence of hysteresis is linked to the capillary condensation of N<sub>2</sub>. Hysteresis is a characteristic of mesoporous adsorbents and confirms the presence of micro and mesopores.<sup>34,35</sup> The pore size distribution curve presented in Figure 4b (and Figure S2) further confirms the microporous and mesoporous nature of all APCs. The figure illustrates pore width maxima occurring at 8.4/9.7/11.1/19.0 Å for *L N-K*, 9.7/12.1/19.8 Å for *L CD-K*, 8.4 Å for *L N-CD*, 19.0 Å for *L CD*, 8.1/9.2/11.6 Å for *L N-KCD*, 9.2/19.0 Å for *L CD-KCD*, 8.4/9.7/19.0 Å for *L N-Z*, 9.7/19.0 Å for *L CD-Z*, 8.4/9.7/19.0 Å for



*L N-ZCD* and 8.4/9.2/19.0 Å for *L CD-ZCD*. For all the APCs, the pore diameter of ~8 Å available in the pore size distribution curves was large enough to accommodate CO<sub>2</sub> with a kinetic diameter of 3.3 Å.<sup>36</sup> This is crucial for efficient CO<sub>2</sub> capture. Pore width maxima centred at 19 Å were common in *L CD* and APCs derived from the secondary activation of *L CD*, such as *L CD-Z* and *L CD-ZCD*. This indicated the absence of a pore-widening effect during secondary chemical activation using ZnCl<sub>2</sub> and physicochemical activation using ZnCl<sub>2</sub> + CO<sub>2</sub>. In contrast, the secondary chemical activation of *L CD* using KOH resulted in pore widening, and the maxima shifted to 19.8 Å. The pore size distribution curves suggested that the secondary activation of *L CD* via both chemical and physicochemical activation resulted in the formation of additional micropores.

Table 2 lists the yields and key textural properties of the *L*-based APCs. The conversion yield of the raw biomass to APC ranged within 14.5-40.8 wt.%. The highest  $S_{\text{BET}}$  of 1480 m<sup>2</sup>/g and maximum total pore volume of 0.737 cm<sup>3</sup>/g were obtained for the APC produced via the physicochemical activation of *L N* using KOH+CO<sub>2</sub>. In contrast, the chemical activation of *L N* using KOH promoted the formation of micropores, achieving a micro-porosity ( $\phi_{\text{micro}}$ ) as high as 97.74%. Physicochemical or chemical treatment of *L N* led to better porosity than the identical treatment of *L CD* did. For example, chemical activation of *L N* using KOH resulted in  $S_{\text{BET}}$  of 1108 m<sup>2</sup>/g, which is considerably higher than that for the chemical activation of *L CD* using KOH. This could be attributed to the relatively higher processing temperature of *L CD* (i.e., 800 °C), leading to the formation of a sturdy aromatic structure, which could be less susceptible to further activation. For *L N*, combined physical and chemical activation (using KOH + CO<sub>2</sub> and ZnCl<sub>2</sub> + CO<sub>2</sub>) produced better porosity than physical activation (using CO<sub>2</sub>) and chemical activation (using KOH and ZnCl<sub>2</sub>) alone. Compared to KOH activation, physicochemical activation with KOH + CO<sub>2</sub> increased the  $S_{\text{BET}}$  by 33% and the total pore volume by 31%. However,  $S_{\text{BET}}$  and total pore volume were improved by ~12% and 10%, respectively, for physicochemical activation using ZnCl<sub>2</sub> + CO<sub>2</sub> compared to activation with ZnCl<sub>2</sub> only. A similar trend was reported in.<sup>24,28,37</sup> For lignin-based APCs, the percentage of micropore volume ( $f_{\text{micro}}$ ) ranged from 81 to 93%, indicating the dominance of micropores. Micropores are desired for better CO<sub>2</sub> capture.



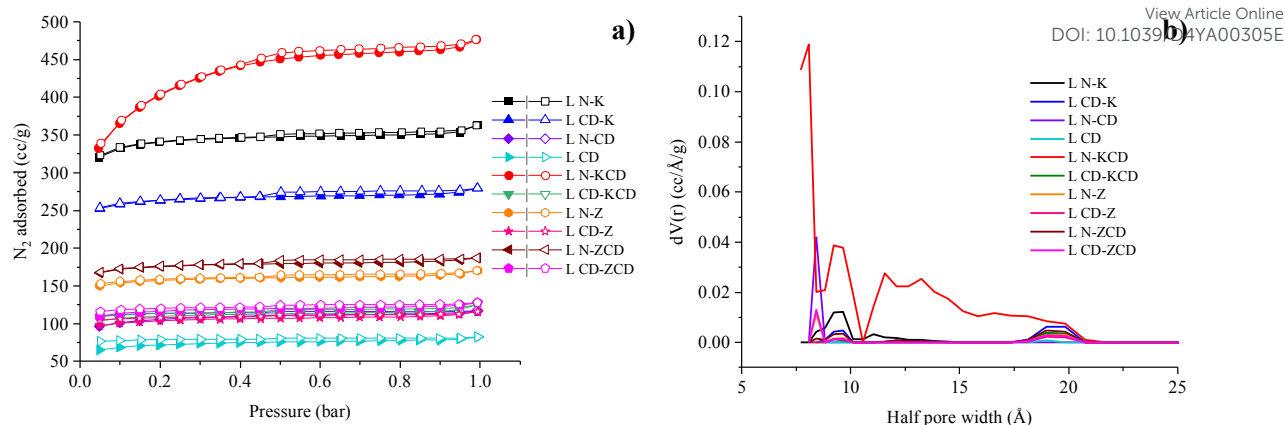


**Figure 4.** (a)  $N_2$  adsorption/desorption isotherms of lignin-based activated porous carbons at  $-196\text{ }^\circ\text{C}$  (solid symbols represent adsorption and hollow symbols indicates desorption), (b) pore size distribution from NLDFT method using  $N_2$  isotherms at  $-196\text{ }^\circ\text{C}$ .

**Table 2.** Yield and textural properties of activated carbons derived from lignin protobind 2400 at varied conditions.

	Yield, wt. %	$S_{\text{BET}}$ , $\text{m}^2/\text{g}$	$S_{\text{micro}}$ , $\text{m}^2/\text{g}$	$\phi_{\text{micro}}$ , %	$R_{\text{avg}}$ , nm	$V_{\text{T}}$ , $\text{cm}^3/\text{g}$	$V_{\text{micro}}$ , $\text{cm}^3/\text{g}$	$f_{\text{micro}}$ , %
<i>L N-KCD</i>	14.54	1480	1383	93.45	0.995	0.737	0.597	81.00
<i>L N-K</i>	28.96	1108	1083	97.74	1.014	0.562	0.515	91.64
<i>L CD</i>	40.82	269	257	95.53	0.946	0.127	0.107	84.25
<i>L CD-K</i>	35.28	844	826	97.87	1.024	0.432	0.400	92.59
<i>L N-CD</i>	35.36	399	385	96.49	0.908	0.181	0.159	87.84
<i>L CD-KCD</i>	30.09	353	338	95.75	1.093	0.193	0.163	84.46
<i>L N-Z</i>	38.93	504	491	97.42	1.045	0.264	0.237	89.77
<i>L CD-Z</i>	31.82	334	322	96.40	1.071	0.180	0.155	86.11
<i>L N-ZCD</i>	37.19	564	551	97.70	1.026	0.290	0.266	91.72
<i>L CD-ZCD</i>	31.82	377	364	96.55	1.051	0.198	0.175	88.38

$S_{\text{BET}}$  = Specific BET surface area

$S_{\text{micro}}$  = Micro-pore area using t-plot method

$\phi_{\text{micro}}$  = Micro-porosity, % =  $(S_{\text{micro}}/S_{\text{BET}}) \times 100$

$R_{\text{avg}}$  = Average pore radius

$V_{\text{T}}$  = Estimated at a relative pressure  $P/P_0 = 0.99$

$V_{\text{micro}}$  = Micropore volume estimated using t-plot method

$f_{\text{micro}}$  = Percentage of micro-pore volume, % =  $(V_{\text{micro}}/V_{\text{T}}) \times 100$

### 3.3 $\text{CO}_2$ adsorption characteristics

$\text{CO}_2$  and  $\text{N}_2$  adsorption isotherms were recorded at 0, 25 and 40  $^\circ\text{C}$  up to 1 bar (Table 3).  $\text{CO}_2$  uptake values at 0.1-0.15 bar are also listed in the Table 3. Low-pressure  $\text{CO}_2$  uptake at 0.1-0.15 bar is vital as it represents the realistic partial pressure of  $\text{CO}_2$  in the flue gas.<sup>38</sup> Figure





5a-c demonstrates CO<sub>2</sub> adsorption isotherms at three different temperatures. At 1 bar, saturation in terms of CO<sub>2</sub> uptake was absent for *L N-K*, *L CD-K* and *L N-KCD*, indicating more CO<sub>2</sub> uptake at elevated adsorption pressure. It was consistent over the range of tested adsorption temperatures. The absence of hysteresis indicated that CO<sub>2</sub> adsorption followed Type I isotherms, which further advocates the microporous nature of the APCs.

Despite having higher  $S_{\text{BET}}$  for physicochemical activated APC (i.e., *L N-KCD*), it indicated lower CO<sub>2</sub> adsorption capacity than chemically activated APC (i.e., *L N-K*). It indicates non-linearity between  $S_{\text{BET}}$  and CO<sub>2</sub> adsorption capacity, which was commonly observed.<sup>7,28,39,40</sup> Conversely, combined physical and chemical activation using ZnCl<sub>2</sub> + CO<sub>2</sub> slightly improved CO<sub>2</sub> uptake compared to individual physical or chemical activation using CO<sub>2</sub> or ZnCl<sub>2</sub>, respectively. APCs derived via chemical activation using KOH resulted in the highest CO<sub>2</sub> adsorption capacity. The maximum CO<sub>2</sub> adsorption capacity of 5.68 mmol/g at 0 °C/1 bar was observed for *L N-K*. At lower adsorption pressure, *L CD-K* exhibited better CO<sub>2</sub> adsorption than *L N-K*. However, CO<sub>2</sub> adsorption capacity of *L N-K* starts surpassing that of *L CD-K* above adsorption pressure of 0.5 bar. The observation was consistent over the range of adsorption temperature studied. This could be attributed to the superior microporosity of *L CD-K* as micropores are likely to get occupied first at lower adsorption pressure. Two-step physical activation yield slightly better CO<sub>2</sub> adsorption performance than one-step physical activation. Energy penalty during two-step physical activation is yet to be justified by a marginal increase in CO<sub>2</sub> adsorption. From a better CO<sub>2</sub> uptake perspective, the performance of the type of activating agents can be ranked as: KOH > KOH + CO<sub>2</sub> > ZnCl<sub>2</sub> + CO<sub>2</sub> > ZnCl<sub>2</sub> > CO<sub>2</sub>. Table 4 compares the CO<sub>2</sub> adsorption capacity of APCs derived from various biomass precursors.

A linear relationship between CO<sub>2</sub> uptake and textural properties (i.e.,  $S_{\text{BET}}$ ,  $S_{\text{micro}}$ ,  $\phi_{\text{micro}}$ ,  $R_{\text{avg}}$ ,  $V_{\text{T}}$ ,  $V_{\text{micro}}$ , and  $f_{\text{micro}}$ ) is presented in Figure S3 to better understand the parameters affecting the CO<sub>2</sub> adsorption performance of APC. No clear trend was observed between any of the textural properties and CO<sub>2</sub> uptake. It implied that CO<sub>2</sub> adsorption on the APC surface is affected by multiple parameters.<sup>41</sup>

### 3.4 Selectivity and heat of adsorption

For practical on-field gas separation applications, better CO<sub>2</sub> uptake along with higher CO<sub>2</sub>/N<sub>2</sub> selectivity is desired. A CO<sub>2</sub>/N<sub>2</sub> volume ratio of 15:85 was assumed, and ideal adsorption solution theory was applied to determine CO<sub>2</sub> over N<sub>2</sub> selectivity at 0, 25, and 40 °C/1 bar. Adsorption isotherms of single component were fitted into Langmuir-Freundlich isotherm model Eq.(1) and resulting parameters were fitted to Eq.(2).

$$Q = \frac{q_{\text{sat}} * k * c^n}{1 + k * c^n}$$

Equation 1



$$S = \frac{q_{CO_2}/q_{N_2}}{p_{CO_2}/p_{N_2}}$$

View Article Online  
DOI: 10.1039/D4YA00305E  
Equation 2

where,  $S$  is  $CO_2/N_2$  selectivity,  $q$  is the amount of  $i^{\text{th}}$  gas adsorbed and  $p$  is the relative pressure of the  $i^{\text{th}}$  gas.

Table 3 lists  $CO_2/N_2$  selectivity for all the APCs, which ranged within 11.9-20.4. A clear trend between selectivity and adsorption temperature was absent. Higher polarizability, quadrupole moment, critical temperature, and lower kinetic diameter for  $CO_2$  than  $N_2$ , favoured better adsorption of  $CO_2$  on the APC surface.<sup>42</sup> Also, being an electrophilic molecule,  $CO_2$  strongly interacts with heteroatom-containing functional groups of APCs.

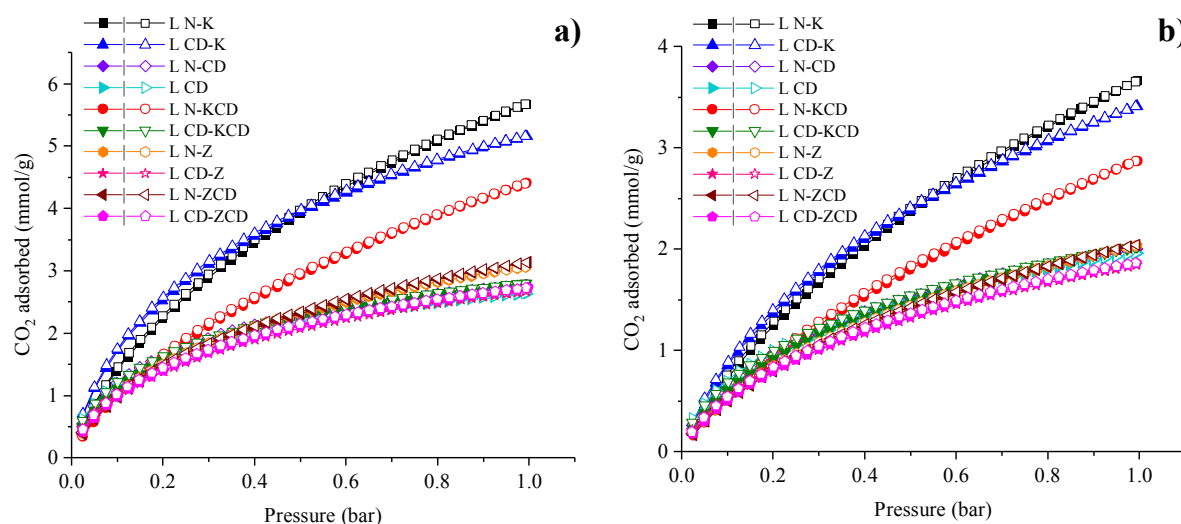
Isosteric heat of adsorption ( $q_{st}$ ) measures the strength of adhesion between adsorbent and adsorbate, which is linked to ease of regeneration of the adsorbent. Table 3 lists  $q_{st}$  values of all the APCs at lower  $CO_2$  loading, which ranged within ~20-33 kJ/mol. The  $q_{st}$  value is inversely proportional to the energy required during the regeneration of the adsorbent. For all the APCs,  $q_{st} < 40$  kJ/mol indicated that adsorption predominantly occurred via physisorption through dipole-quadrupole interaction between  $CO_2$  and APC surface. Secondary activation of biochar prepared in  $CO_2$  indicated higher  $CO_2/N_2$  selectivity and  $q_{st}$  than that of biochar prepared in the  $N_2$  atmosphere. The observation was consistent for all the tested combination of activating agents considered in the study. For example, *L N-K* vs. *L CD-K*, *L N-KCD* vs. *L CD-KCD*, *L N-Z* vs. *L-CD Z* and *L N-ZCD* vs. *L CD-ZCD*.  $CO_2$  carbonization/activation may have modified the surface chemistry of the material or introduced functional groups, leading to stronger interactions with  $CO_2$  molecules. This enhanced interaction can result in a higher heat of adsorption. The similar trend observed for APCs derived from pine sawdust indicates this effect is not much more feedstock sensitive.<sup>28</sup> Figure 5d represents variation in  $q_{st}$  with  $CO_2$  loading. The elevated  $q_{st}$  observed at the minimum  $CO_2$  loading may be explained by a preference for occupying ultrafine pores and/or the adhesion of  $CO_2$  to surface heterogeneity. As  $CO_2$  loading increases, the diminishing trend in the isosteric heat of adsorption can be ascribed to the saturation of strong binding sites. For most of the APCs, a consistently strong correlation with increasing  $CO_2$  loading suggests uniformity in adsorption sites in terms of binding energy. The moderate  $q_{st}$  value indicates convenient regeneration, supporting their suitability for multi-cycle  $CO_2$  adsorption applications. Multi-cyclic  $CO_2$  adsorption at 0 °C was executed for the best-performing APC in terms of  $CO_2$  adsorption i.e., *L N-K* up to 10 cycles. As indicated in Figure 6, a fluctuation of 0.51% in amount of  $CO_2$  adsorbed was observed during 10 consecutive adsorption/desorption cycles. The remarkable stability and reusability of *L N-K* for  $CO_2$  adsorption could be attributed to non-destructive uptake and release. However, its stability towards the actual flue gas scenario has yet to be tested.

As of 2023, approximately 40 commercial  $CO_2$  capture facilities are actively operating worldwide, with a total annual capture capacity exceeding 45 Mt of  $CO_2$ . Despite the announcement of over 50 upcoming capture facilities scheduled to commence operations by



2030, declared since January 2022, the current project pipeline only represents roughly one-third of the anticipated requirement for achieving net-zero emissions by 2030. Noteworthy advancements have also been observed in the application of CCUS within the industrial sector. In 2022, several new projects were commissioned, encompassing the integration of CCUS into sectors such as iron, steel, fertilizer, and other chemical production processes. Projections indicate that approximately 25 biomass and waste-fired combined heat and power plants could be responsible for capturing around 30 Mt of CO<sub>2</sub> by the year 2030. Considering the ongoing project pipeline, it is anticipated that by 2030, the annual capture capacity, derived from both new constructions and retrofits, could reach around 90 Mt of CO<sub>2</sub> from hydrogen production, approximately 80 Mt from power generation, and roughly 35 Mt from various industrial facilities, including cement and steel production.<sup>43</sup>

In the wider spectrum, utilization of APC for post-combustion CO<sub>2</sub> capture presents invaluable benefits such as compatibility to current energy systems, easy scalability, and steady operation. APC can be employed in packed-bed adsorption systems, known for their simplicity and straightforward scalability. APC derived from green and renewable sources can effectively capture CO<sub>2</sub> emissions from industries heavily reliant on coal, including cement, chemical, oil refineries, and steel. As per the technical report from the National Energy Technology Laboratory (NETL), an adsorbent proves practical and economically viable for CO<sub>2</sub> capture if it demonstrates an isothermal CO<sub>2</sub> adsorption capacity exceeding 3 mmol/g at 25 °C and 1 bar.<sup>44</sup> The *L N-K*, as indicated, exhibits an isothermal CO<sub>2</sub> adsorption capacity of 3.66 mmol/g at 25 °C and 1 bar, signifying its suitability for commercial operations. Along with CO<sub>2</sub> capture applications, the conversion of lignin into a stable form of APC restricts the release of carbon into the atmosphere.



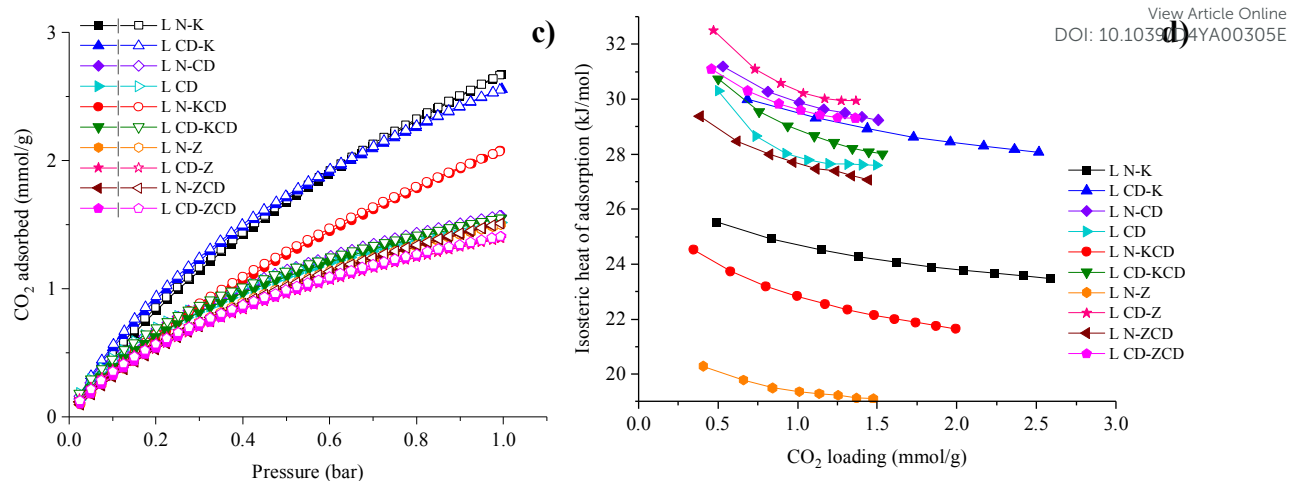


**Figure 5.** CO<sub>2</sub> adsorption isotherms at (a) 0 °C, (b) 25 °C, and (c) 40 °C (solid symbols represent adsorption, and hollow symbols indicate desorption), and (d) isosteric heat of CO<sub>2</sub> adsorption.



Table 3. Gas adsorption performance of activated carbons at 0, 25, and 40 °C.

Sample	CO <sub>2</sub> adsorption capacity, mmol/g						N <sub>2</sub> adsorption capacity, mmol/g			<i>q</i> <sub>st</sub> (kJ/mol)	CO <sub>2</sub> /N <sub>2</sub> selectivity		
	1 bar			0.1 (0.15) bar			0 °C	25 °C	40 °C		0 °C	25 °C	40 °C
	0 °C	25 °C	40 °C	0 °C	25 °C	40 °C							
<i>L N-K</i>	5.68	3.66	2.67	1.38 (1.84)	0.72 (1.00)	0.46 (0.66)	0.88	0.52	0.34	25.53	13.52	12.56	12.50
<i>L CD-K</i>	5.16	3.41	2.56	1.73 (2.17)	0.85 (1.12)	0.54 (0.73)	0.75	0.46	0.30	29.99	18.51	16.09	16.14
<i>L N-CD</i>	2.77	2.00	1.57	1.16 (1.40)	0.61 (0.79)	0.40 (0.54)	0.50	0.29	0.18	31.20	18.20	18.10	20.39
<i>L CD</i>	2.64	1.96	1.52	1.07 (1.31)	0.61 (0.79)	0.39 (0.53)	0.47	0.28	0.18	30.31	17.69	17.88	18.79
<i>L N-KCD</i>	4.40	2.87	2.08	0.99 (1.31)	0.52 (0.73)	0.34 (0.48)	0.66	0.40	0.26	24.53	12.97	11.86	11.97
<i>L CD-KCD</i>	2.80	2.02	1.55	1.11 (1.34)	0.61 (0.78)	0.39 (0.53)	0.47	0.28	0.17	30.74	18.21	18.58	19.92
<i>L N-Z</i>	3.06	2.03	1.50	1.00 (1.26)	0.51 (0.67)	0.32 (0.44)	0.49	0.29	0.17	20.29	16.45	15.15	17.17
<i>L CD-Z</i>	2.67	1.84	1.39	0.97 (1.20)	0.50 (0.66)	0.32 (0.43)	0.44	0.26	0.16	32.51	17.71	16.50	17.82
<i>L N-ZCD</i>	3.14	2.04	1.51	0.97 (1.24)	0.50 (0.65)	0.31 (0.43)	0.48	0.29	0.18	29.38	16.53	14.57	15.84
<i>L CD-ZCD</i>	2.73	1.87	1.41	0.98 (1.21)	0.51 (0.67)	0.33 (0.44)	0.45	0.27	0.17	31.10	17.46	16.13	17.17

Table 4. Comparison of CO<sub>2</sub> adsorption performance of activated porous carbon derived via chemical activation of various biomass precursors.

Precursor (P)	Activating agent (AA)	Impregnation ratio (P:AA)	Carbonization (C) & activation conditions (A) (T (°C)/residence time (min.))	Yield (wt.%)	<i>S</i> <sub>BET</sub> (m <sup>2</sup> /g)	<i>V</i> <sub>t</sub> (cm <sup>3</sup> /g)	CO <sub>2</sub> adsorption conditions		CO <sub>2</sub> adsorption capacity (mmol/g)	<i>q</i> <sub>st</sub> (kJ/mol)	Selectivity (CO <sub>2</sub> /N <sub>2</sub> ) <sup>e</sup>	Ref.
							T (°C)	P (bar)				
Bamboo shoot shells <sup>b</sup>	CaCl <sub>2</sub>	1:1	C <sup>c</sup> -600/120 A-700/120	-	541	0.24	0/25	1/1	3.14/2.39	35.0	-	45
Bamboo shoot shells + urea <sup>b</sup>	K <sub>2</sub> CO <sub>3</sub>	1:3	C <sup>c</sup> -500/120 A-800/-	-	1958	0.83	0/25	1/1	7.52/3.60	33.0	14.0	46
Chitosan <sup>a</sup>	KOH	3:2	A-700/60	-	1506	0.64	0/25	1/1	6.91/4.40	32.5	21.0	47





Coconut shells <sup>b</sup>	K <sub>2</sub> S <sub>2</sub> O <sub>3</sub>	1:1	C <sup>c</sup> - A-700/60	-	1188	0.47	0/25	1/1	5.31/3.59	35.0	20.0	48
Coconut shells <sup>b</sup>	K <sub>2</sub> S <sub>2</sub> O <sub>8</sub>	1:1	C <sup>c</sup> -500/120 A-750/120	-	581	0.26	0/25	1/1	3.77/2.56	39.0	17.0	49
Coconut shell <sup>b</sup>	KOH	1:3	C <sup>c</sup> -500/120 A-600/60	-	1172	0.44	0/25	1/1	6.04/4.23	37.0	22.0	50
Corn cob <sup>b</sup>	KOH	1:3	C <sup>d</sup> -230/480	16.3	2716	0.71	15	1	4.50	24.1	-	51
	ZnCl <sub>2</sub>	1:3	A-600/60	18.9	1567	0.48	15	1	3.64	17.7	-	
	H <sub>3</sub> PO <sub>4</sub>	1:3		17.3	2314	0.59	15	1	2.95	9.3	-	
Cotton bolls <sup>b</sup>	KOH	1:2	C <sup>c</sup> -500/60 A-700/90	23.3	1381	-	25	1	5.14	-	-	52
Garlic peel <sup>b</sup>	KOH	1:2	C <sup>d</sup> -200/1440 A-800/60	-	1262	0.70	0/25	1/1	4.33/2.82	-	-	53
Lotus seeds <sup>b</sup>	KOH	1:3	C <sup>c</sup> -600/120 A-800/120	-	2230	0.96	0/25	1/1	6.80/3.10	30.4	-	54
Macadamia nutshell <sup>b</sup>	KOH	1:1.7	C <sup>c</sup> -500/120 A-771/150	-	1417	0.75	0/25/40	1/1/1	6.58/3.94/3.15	27.0	-	55
Slash pine <sup>a</sup>	KOH	1:4	A-580/120	19.5	1185	0.35	0/15	1	4.93/3.86	39.7	-	56
Pine sawdust <sup>b</sup>	KOH	1:2	C <sup>c</sup> -600/90 A-800/90	19.89	1319	0.66	0/25/40	1/1/1	6.35/3.82/2.81	24.9	11.8	28
Lignin protobind 2400 <sup>b</sup>	KOH	1:2	C <sup>c</sup> -600/90 A-800/90	28.96	1108	0.56	0/25/40	1/1/1	5.68/3.66/2.67	25.5	12.6	<b>Present study</b>

<sup>a</sup> Direct activation

<sup>b</sup> Two-step activation

<sup>c</sup> Pyrolytic carbonization

<sup>d</sup> Hydrothermal carbonization

<sup>e</sup> at 25 °C

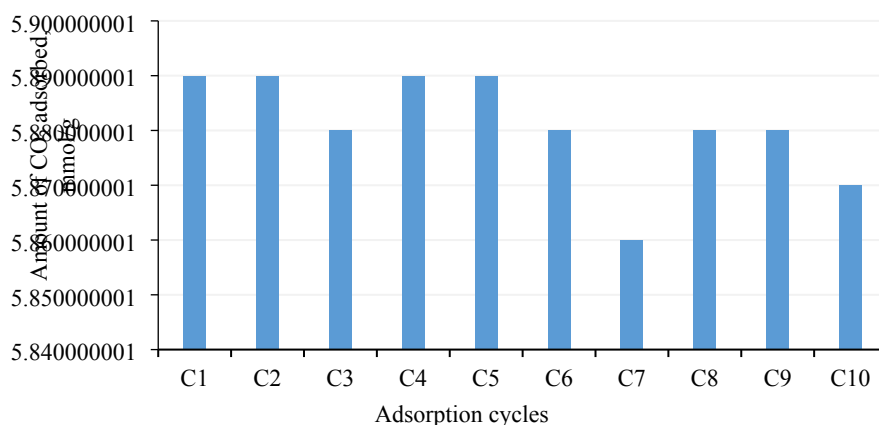


**Figure 6.** Multi-cyclic CO<sub>2</sub> adsorption performance of *L N-K* at 0 °C.

## 4 Conclusion

Lignin protobind 2400 was converted to a value-added product, activated porous carbon (APC) using combined activating agents KOH + CO<sub>2</sub> and ZnCl<sub>2</sub> + CO<sub>2</sub>. Also, the effectiveness of the combined physicochemical activation with individual chemical and physical activating agents was compared. Although KOH + CO<sub>2</sub> activation improved BET surface area by 33% compared to only KOH activation, CO<sub>2</sub> uptake for KOH + CO<sub>2</sub> activation decreased by 23%, compared to only KOH activation. On the other hand, physicochemical activation using ZnCl<sub>2</sub> + CO<sub>2</sub> slightly improved BET surface area as well as CO<sub>2</sub> uptake compared to only ZnCl<sub>2</sub> and only CO<sub>2</sub> activation. From a better CO<sub>2</sub> uptake perspective, the performance of the type of activating agents can be ranked as: KOH > KOH + CO<sub>2</sub> > ZnCl<sub>2</sub> + CO<sub>2</sub> > ZnCl<sub>2</sub> > CO<sub>2</sub>. Secondary activation of biochar carbonized in the N<sub>2</sub> atmosphere offered better BET surface area and increased CO<sub>2</sub> uptake compared to that of biochar carbonized in the CO<sub>2</sub> atmosphere. Considerably, higher CO<sub>2</sub>/N<sub>2</sub> selectivity and isosteric heat of CO<sub>2</sub> adsorption were observed for APC derived from secondary activation of biochar carbonized in a CO<sub>2</sub> environment than in N<sub>2</sub> environment. The combination of better CO<sub>2</sub> adsorption capacity, lower heat of adsorption, reasonably good CO<sub>2</sub>/N<sub>2</sub> selectivity, and excellent reusability/stability of lignin-based APC supported its utilization for post-combustion CO<sub>2</sub> capture.

## Declaration of Competing Interest

The authors declare that they have no known competing financial interests or personal relationships that could have appeared to influence the work reported in this paper.

## CRedit authorship contribution statement



**Himanshu Patel:** Methodology, Validation, Formal analysis, Investigation, Writing – original draft. **Amar Mohanty:** Conceptualization, Resources, Supervision, Investigation, Validation, Writing – review & editing. **Manjusri Misra:** Conceptualization, Methodology, Funding acquisition, Project administration, Resources, Supervision, Investigation, Validation, Writing – review & editing.

View Article Online

DOI: 10.1089/EA.2024.00305E

## Acknowledgments

The authors would like to thank the financial support of (i) the Ontario Agri-Food Innovation Alliance – Bioeconomy for Industrial Uses Research Program (Project Nos. 030648 and 030671); (ii) the Natural Sciences and Engineering Research Council of Canada (NSERC), Canada Discovery Grants Program Project No. 401716; and (iii) NSERC Alliance Grants Program (Project No. 401769) along with the partner industry Competitive Green Technologies, Lamington, Ontario, Canada (Project No. 055427) to carry out this work.

## References

- 1 CDIAAC, *Carbon Dioxide Information Analysis Center.*, 2011.
- 2 B. P. E. Outlook, *London, United Kingdom* 2019.
- 3 W. M. Organization, *WMO Statement on the State of the Global Climate in 2019*, 2020.
- 4 T. R. K. C. Doddapaneni, R. Praveenkumar, H. Tolvanen, J. Rintala and J. Konttinen, *Appl. Energy*, 2018, **213**, 272–284.
- 5 H. Patel, A. Mohanty and M. Misra, *Renew. Sustain. Energy Rev.*, 2024, **199**, 114484.
- 6 X. Yuan, J. Wang, S. Deng, M. Suvarna, X. Wang, W. Zhang, S. T. Hamilton, A. Alahmed, A. Jamal, A.-H. A. Park and others, *Renew. Sustain. Energy Rev.*, 2022, **162**, 112413.
- 7 L. Rao, S. Liu, L. Wang, C. Ma, J. Wu, L. An and X. Hu, *Chem. Eng. J.*, 2019, **359**, 428–435.
- 8 A. Mukherjee, J. A. Okolie, A. Abdelrasoul, C. Niu and A. K. Dalai, *J. Environ. Sci.*, 2019, **83**, 46–63.
- 9 L. Jiang, A. Gonzalez-Diaz, J. Ling-Chin, A. P. Roskilly and A. J. Smallbone, *Appl. Energy*, 2019, **245**, 1–15.
- 10 Y. Guo, C. Tan, J. Sun, W. Li, J. Zhang and C. Zhao, *Chem. Eng. J.*, 2020, **381**, 122736.
- 11 G. Singh, K. S. Lakhi, S. Sil, S. V. Bhosale, I. Kim, K. Albahily and A. Vinu, *Carbon N. Y.*, 2019, **148**, 164–186.
- 12 A. K. Mohanty, S. Vivekanandhan, O. Das, L. M. Romero Millán, N. B. Klinghoffer, A. Nzihou and M. Misra, *Nat. Rev. Methods Prim.*, 2024, **4**, 19.
- 13 J. Becker and C. Wittmann, *Biotechnol. Adv.*, 2019, **37**, 107360.
- 14 U. S. EPA, *United States Environ. Prot. Agency*.
- 15 Z. Wu, J. Zou, Y. Zhang, X. Lin, D. Fry, L. Wang and J. Liu, *Chem. Eng. J.*, 2022, **427**, 131547.
- 16 P. Sirous-Rezaei, D. Creaser and L. Olsson, *Appl. Catal. B Environ.*, 2021, **297**, 120449.
- 17 L. Yu, L. Liang, I. Bajaj, K. Seabright, D. J. Keffer, I. N. Ivanov, H. Chen, S. Dai, A.



- J. Ragauskas, C. T. Maravelias and D. P. Harper, *Carbon N. Y.*, 2023, **213**, 118285. View Article Online  
DOI: 10.1039/D4YA00305E
- 18 Y.-Y. Wang, C. E. Wyman, C. M. Cai and A. J. Ragauskas, *ACS Appl. Polym. Mater.*, 2019, **1**, 1672–1679.
- 19 J. Zhang, L. Yu, Z. Wang, Y. Tian, Y. Qu, Y. Wang, J. Li and H. Liu, *J. Chem. Technol. & Biotechnol.*, 2011, **86**, 1177–1183.
- 20 M. Y. Balakshin, E. A. Capanema, I. Sulaeva, P. Schlee, Z. Huang, M. Feng, M. Borghei, O. J. Rojas, A. Potthast and T. Rosenau, *ChemSusChem*, 2021, **14**, 1016–1036.
- 21 H. Luo and M. M. Abu-Omar, *Encycl. Sustain. Technol.*, 2017, **3**, 573–585.
- 22 D. V. Cuong, N.-L. Liu, V. A. Nguyen and C.-H. Hou, *Sci. Total Environ.*, 2019, **692**, 844–853.
- 23 D. V. Cuong and C.-H. Hou, *J. Taiwan Inst. Chem. Eng.*, 2022, **139**, 104533.
- 24 K. Adlak, R. Chandra, V. K. Vijay and K. K. Pant, *J. Anal. Appl. Pyrolysis*, 2021, **155**, 105102.
- 25 S. Balou, S. E. Babak and A. Priye, *ACS Appl. Mater. & Interfaces*, 2020, **12**, 42711–42722.
- 26 A. D. Igalavithana, S. W. Choi, P. D. Dissanayake, J. Shang, C.-H. Wang, X. Yang, S. Kim, D. C. W. Tsang, K. B. Lee and Y. S. Ok, *J. Hazard. Mater.*, 2020, **391**, 121147.
- 27 J. Serafin, B. Dziejarski, X. Vendrell, K. Kielbasa and B. Michalkiewicz, *Biomass and Bioenergy*, 2023, **175**, 106880.
- 28 H. Patel, H. Weldekidan, A. Mohanty and M. Misra, *Carbon Capture Sci. & Technol.*, 2023, 100128.
- 29 S. Sahoo, M. Ö. Seydibeyoğlu, A. K. Mohanty and M. Misra, *Biomass and Bioenergy*, 2011, **35**, 4230–4237.
- 30 N. A. Ahmad, K. A. Al-attab, Z. A. Zainal and P. Lahijani, *Bioresour. Technol. Reports*, 2021, **15**, 100785.
- 31 H. Weldekidan, H. Patel, A. Mohanty and M. Misra, *Carbon Capture Sci. Technol.*, 2024, **10**, 100149.
- 32 S. Rani, E. Padmanabhan and B. K. Prusty, *J. Pet. Sci. Eng.*, 2019, **175**, 634–643.
- 33 W. Wu, C. Wu, G. Zhang, J. Liu, Y. Li and G. Li, *Fuel*, 2023, **332**, 126107.
- 34 S. Charola, H. Patel, S. Chandna and S. Maiti, *J. Clean. Prod.*, , DOI:10.1016/j.jclepro.2019.03.169.
- 35 J. Rouquerol, D. Avnir, C. W. Fairbridge, D. H. Everett, J. M. Haynes, N. Pernicone, J. D. F. Ramsay, K. S. W. Sing and K. K. Unger, *Pure Appl. Chem.*, 1994, **66**, 1739–1758.
- 36 Y.-S. Bae and C.-H. Lee, *Carbon N. Y.*, 2005, **43**, 95–107.
- 37 K. Kielbasa, S. Sahin Bayar, E. A. Varol, J. Sreńscek-Nazzal, M. Bosacka and B. Michalkiewicz, *Ind. Crops Prod.*, 2022, **187**, 115416.
- 38 B. Ashourirad, P. Arab, T. Islamoglu, K. A. Cychosz, M. Thommes and H. M. El-Kaderi, *J. Mater. Chem. A*, 2016, **4**, 14693–14702.
- 39 M. Singh, N. Borkhatariya, P. Pramanik, S. Dutta, S. K. Ghosh, P. Maiti, S. Neogi and S. Maiti, *J. CO2 Util.*, 2022, **60**, 101975.
- 40 B. Zhao, M. Borghei, T. Zou, L. Wang, L.-S. Johansson, J. Majoinen, M. H. Sipponen, M. Österberg, B. D. Mattos and O. J. Rojas, *ACS Nano*, 2021, **15**, 6774–6786.
- 41 C. Wu, J. Liu, Y. Wang, Y. Zhao, G. Li and G. Zhang, *Sep. Purif. Technol.*, 2024, **329**, 125188.
- 42 P. Pramanik, H. Patel, S. Charola, S. Neogi and S. Maiti, *J. CO2 Util.*, , DOI:10.1016/j.jcou.2021.101450.
- 43 I. 2023, *Tracking Clean Energy Progress 2023*, Paris, 2023.
- 44 H. W. Pennline, *Sorbent Research for the Capture of Carbon Dioxide*, 2016.



- 45 W. Wu, C. Wu, G. Zhang and J. Liu, *J. Anal. Appl. Pyrolysis*, 2022, **168**, 105742. View Article Online  
DOI: 10.1039/D4YA00305E
- 46 W. Wu, C. Wu, J. Liu, H. Yan, G. Zhang, G. Li, Y. Zhao and Y. Wang, *Fuel*, 2024, **363**, 130937.
- 47 J. Shao, J. Wang, Q. Yu, F. Yang, M. Demir, O. C. Altinci, A. Umay, L. Wang and X. Hu, *Sep. Purif. Technol.*, 2024, **333**, 125891.
- 48 J. Bai, J. Shao, Q. Yu, M. Demir, B. Nazli Altay, T. Muhammad Ali, Y. Jiang, L. Wang and X. Hu, *Chem. Eng. J.*, 2024, **479**, 147667.
- 49 C. Liu, Y. Zhi, Q. Yu, L. Tian, M. Demir, S. G. Colak, A. A. Farghaly, L. Wang and X. Hu, *ACS Appl. Nano Mater.*
- 50 J. Yang, L. Yue, X. Hu, L. Wang, Y. Zhao, Y. Lin, Y. Sun, H. DaCosta and L. Guo, *Energy & Fuels*, 2017, **31**, 4287–4293.
- 51 A. Sarwar, M. Ali, A. H. Khoja, A. Nawar, A. Waqas, R. Liaquat, S. R. Naqvi and M. Asjid, *J. CO<sub>2</sub> Util.*, 2021, **46**, 101476.
- 52 H. Patel, H. Mangukiya, P. Maiti and S. Maiti, *J. Clean. Prod.*, 2020, 125738.
- 53 G. Huang, Y. Liu, X. Wu and J. Cai, *New Carbon Mater.*, 2019, **34**, 247–257.
- 54 G. Singh, K. S. Lakhi, K. Ramadass, C. I. Sathish and A. Vinu, *ACS Sustain. Chem. Eng.*, 2019, **7**, 7412–7420.
- 55 C. Wu, G. Zhang, J. Liu, H. Yan and Y. Lv, *Int. J. Energy Res.*, 2022, **46**, 17204–17219.
- 56 M. B. Ahmed, M. A. H. Johir, J. L. Zhou, H. H. Ngo, L. D. Nghiem, C. Richardson, M. A. Moni and M. R. Bryant, *J. Clean. Prod.*, 2019, **225**, 405–413.





## Data Availability Statement

View Article Online  
DOI: 10.1039/D4YA00305E

Data for this article, including Raw/processed/metadata files are available at 'Open Science Framework' at [https://osf.io/kqfuy/?view\\_only=7cda4a7a86174137b9f1ecc2548dc5ce](https://osf.io/kqfuy/?view_only=7cda4a7a86174137b9f1ecc2548dc5ce).

